International Journal of Heat and Mass Transfer 248 (2025) 127139

Contents lists available at ScienceDirect

International Journal of Heat and Mass Transfer

journal homepage: www.elsevier.com/locate/hmt

Investigating the performance of a heat sink for satellite avionics thermal management: From ground-level testing to space-like conditions ☆

Laryssa Sueza Raffa [a,*], Matt Ryall [b], Iver Cairns [d], Nick S. Bennett [a], Lee Clemon [a,c]

[a] School of Mechanical and Mechatronic Engineering, University of Technology Sydney, Ultimo, NSW 2007, Australia
[b] Mawson Rovers, Eveleigh, NSW 2015, Australia
[c] Mechanical Science and Engineering, The Grainger College of Engineering, University of Illinois Urbana-Champaign, Urbana, IL 61801, USA
[d] ARC Training Centre for Cubesats, UAVs & their applications, University of Sydney, Camperdown, NSW 2050, Australia

ARTICLE INFO

Keywords:
Experiment
Heat sink
Thermal management
Vacuum
Satellite avionics

ABSTRACT

The thermal management of electronics in space presents unique challenges due to high waste heat generation, miniaturised device footprints, and the absence of convective cooling in vacuum environments. This study investigates the behaviour of a metallic heat sink under varying pressure conditions, from atmospheric pressure to high-grade vacuum, using experimental and numerical approaches. The thermal response of a stainless steel heat sink featuring plate fins was investigated at two power levels to simulate different heat loads of satellite avionics. The experiments revealed a significant rise in operating temperatures under lower pressure conditions, with temperatures in high-grade vacuum exceeding those at atmospheric pressure by up to 66%. A reduced-order numerical model was formulated and validated against experimental data, demonstrating strong agreement and providing an efficient tool for predicting heat sink performance in vacuum conditions. The findings underscore the critical impact of pressure on heat dissipation mechanisms and highlight the need for advanced thermal management strategies tailored for space applications. This work contributes to the understanding of heat sink behaviour across varying pressure environments, offering insights for the design of more effective thermal control in aero- and astrospace technologies.

1. Introduction

The advancements of modern electronics has led to devices with greater computational power and smaller footprints, which results in a significant increase in waste heat generation and often insufficient available surface area to dissipate heat [1]. A 10 °C increase in temperature can lead to a twofold rise in electronic component failure rates [2], while even a slight reduction of 1 °C in operating temperature has been shown to improve reliability by decreasing failure rates by 4% [3]. In space applications, the absence of air to promote convective cooling makes thermal regulation even more challenging. Managing heat effectively in such environments is critical to ensuring the functionality of spacecraft electronics, as excessive temperatures pose a serious threat to mission success [4]. Thermal failures been linked to multiple partial or total mission failure events [5,6], emphasising the need for effective thermal control strategies to enhance satellite reliability.

Heat sinks are commonly used for thermal management of electronics, by increasing surface area and enhancing heat rejection to the surroundings. Despite the extensive use of heat sinks in terrestrial applications at atmospheric conditions, limited experimental research has been conducted to understand their performance under conditions typical of space, such as low-pressure or vacuum conditions [7]. Many studies focus on optimising fin geometry, material properties, and other parameters for atmospheric environments [8–11]. However, in vacuum convective cooling is negligible, leading to significantly different thermal behaviours.

Preliminary investigations into heat sink performance under reduced pressures, where both convection and radiation play a role in

☆ This research was funded by the University of Technology Sydney, SmartSat Cooperative Research Centre, the Australian Research Council Training Centre for CubeSats, UAVs, and Their Applications (CUAVA) via grant IC170100023, the Waratah Seed project - partially funded by Investment NSW -, and the Australian Government Research Training Program.

The authors extend their gratitude to the National Space Test Facility at The Australian National University (ANU) for facilitating the thermal performance tests conducted in the Wombat-XL thermal vacuum chamber, with special thanks to Dr Eduardo Trifoni. Last but not least, they sincerely appreciate Dr Xueliang Bai and Mr Patrick Oppel from CUAVA for their valuable assistance during these experiments.

* Corresponding author.
E-mail address: laryssa.suezaraffa@uts.edu.au (L. Sueza Raffa).

https://doi.org/10.1016/j.ijheatmasstransfer.2025.127139
Received 19 February 2025; Received in revised form 16 April 2025; Accepted 18 April 2025
Available online 8 May 2025

Nomenclature

English symbols

$\Delta\dot{E}_{heatsink,stored}$	Variation in thermal energy stored in the heat sink per time (W)
A	Surface area (m^2)
C_p	Specific heat capacity (J/kg K)
k_{eff}	Effective thermal conductivity (W/m K)
m	Mass (kg)
$P_{heatsink}$	Power input on heat sink base surface (W)
P_{heater}	Heater power (W)
P_{loss}	Power losses through assembly mount(W)
$q_{heatsink,conv}$	Power dissipated via convection (W)
$q_{heatsink,rad}$	Power dissipated via radiation (W)
R	Heater resistance (Ω)
T	Temperature (°C)
t	Time (s)
U	Voltage (V)
V_{metal}	Volume of metal material in the heat sink (m^3)
V_{void}	Volume of the internal empty space inside the heat sink (m^3)

Greek symbols

ϵ	Emissivity
ρ	Density (kg/m^3)
σ	Stefan–Boltzmann constant (5.67×10^{-8} W m^{-2} K^{-4})

Subscripts

avg	Average
eff	Effective
top	Referent to the heat sink's top surface
$base$	Referent to the heat sink's base surface
∞	Surroundings

heat dissipation, provide valuable insights. Khor et al. [12] studied the thermal performance of straight fins under natural convection. The study demonstrated that neglecting thermal radiation caused errors in the local convection heat transfer coefficient of over 30%, while excluding the view factor increased errors to more than 60%. Other studies also highlighted the relevance of radiation in the operation of passively cooled heat sinks [13,14]. Chu et al. [15] studied the thermal performance of triangular finned-heat sinks with alternating layouts, using both experimental and numerical methods in ambient pressures from 400 Pa to atmospheric pressure. The study concluded that fins with alternating layouts promoted more airflow into the heat sink, showing a higher heat transfer coefficient. It also reported that the improvement of the fin layout onto the effective heat transfer coefficient was more significant at atmospheric pressure than at lower pressures. Seidel and Rhee [16] investigated the thermal performance of pin-finned heat sinks at low pressure conditions to simulate the high-altitude environment encountered by military aircraft. The study used a hypobaric chamber to assess the relationship between the Reynolds number and thermal resistance. Tests were conducted at pressures ranging from atmospheric (101 325 Pa) up to pressure equivalent to an altitude of 30,000 m (approximately 1070 Pa). The results highlighted the challenges of maintaining effective heat dissipation at reduced air densities, emphasising the influence of ambient pressure on heat transfer. The performance of a finned metallic heat sink with phase change material was experimentally investigated by Sueza Raffa, et al. [17] under atmospheric condition and low-grade vacuum. The results highlighted significant temperature increases in the low-grade vacuum environment of up to 32.8%. The study demonstrated that the inclusion of phase change material led to a greater reduction in electronics temperatures in vacuum, lowering them 18.0 °C, compared to 12.3 °C at atmospheric pressure.

These studies provide valuable insights into the comparative performance of heat sinks at reduced pressure conditions, however their behaviour under even significantly lower pressures, especially high-grade vacuum remains insufficiently understood. Thermal vacuum testing under high-grade vacuum conditions to replicate orbit-like environments are a crucial step in the "test like you fly" philosophy to validate satellite avionics and payloads prior to flight [18]. Validation prior to launch is a vital step in mitigating the risk associated with the high cost of launching satellites. To the best of the authors knowledge, Wang, et al. [7] is the only publication to date to analyse plane-finned heat sinks under vacuum pressure, focusing on radiation heat transfer in a thermoelectric system. The effects of fin width, length and count was studied through a 3D numerical model simulated under atmospheric pressure and vacuum conditions. The model was validated with an experimental test under atmospheric pressure. The study concluded that radiation heat dissipation in vacuum is primarily influenced by angle factors of fin surfaces, which are amplified by increasing the number of fins, fin length, and fin width, leading to higher heat exchange. Further to improved heat sinks designs, high emissivity coatings have been reported to significantly increase the overall radiative heat transfer [19,20].

This work aims to address this gap by examining the thermal performance of a metallic finned heat sink across a range of pressure conditions, from atmospheric levels to high-grade vacuum. Experiments were conducted to simulate typical satellite electronic loads at two different power levels. Additionally, the transient thermal response of the heat sink was predicted by a reduced-order numerical model with low computational complexity through the use of effective thermal conductivity. The contributions of this research are:

- Experimental evaluation of the behaviour of a metallic heat sink under atmospheric and vacuum pressure levels, including high-grade vacuum.
- Development and validation of a simplified numerical model for predicting the heat sink performance at various pressure levels.
- Insights into the effects of ambient pressure on heat dissipation mechanisms, informing design improvements for space-based thermal management systems.

By focusing on the distinct challenges posed by vacuum environments, this work contributes to a better understanding of heat sink performance in space applications, informs testing interpretation under varying ambient pressure environments, and lays the groundwork for designing more effective thermal management systems.

2. Methodology

2.1. Experimental study

This work evaluates the effectiveness of a metallic heat sink operating under distinct levels of ambient pressure. The stainless steel heat sink, which is illustrated in Fig. 1, was made of SS316L stainless steel utilising the additive manufacturing (AM) technique laser powder bed fusion. AM offers numerous advantages in comparison to conventional fabrication processes, such as enabling complex geometries, reducing total quantity of parts, faster production turnarounds [21]. Possible issues linked to additively manufactured components include residual stress-induced distortions and defects such as porosity and cracks [22]. To improve quality and minimise negative effects on thermal properties, post-fabrication assessment is crucial [23]. SS316L is a widely

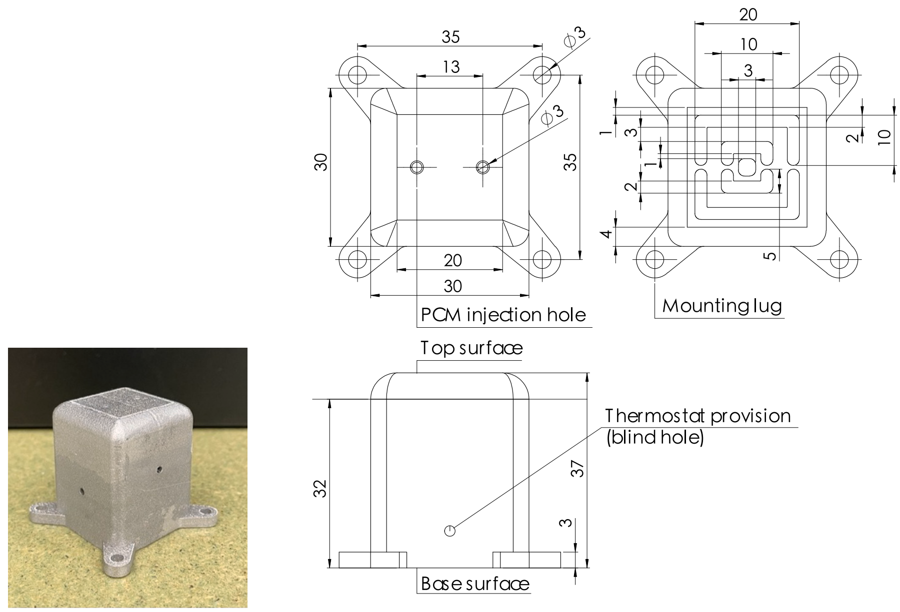

(a) Picture of fabricated heat sink

(b) Drawing of the heat sink design

Fig. 1. (a) Picture of fabricated heat sink and (b) drawing of the heat sink design.

used material in this additive manufacturing technique and has been extensively studied for heat transfer and latent heat energy storage applications [24]. In addition to its thermal properties, it offers strong corrosion resistance and radiation shielding, making it well suited for space environments. The dimensions and weight of the planar-finned heat sink were 30 × 30 × 37 mm and 150.0 g, respectively.

A 30 × 30 mm flat square-shaped electric heater integrated onto a printed circuit board (PCB) was used as a replica for the heat generated by satellite electronics. The PCB was developed by Mawson Rovers, along with its control software. The heater is controlled by a BeagleBone Black microprocessor, which also collects the thermistors recordings. The data is displayed live from an online dashboard, providing cloud data storage, and heater control functionalities. The experimental setup is shown in Figs. 2(a) and 2(b). The PCB features five thermistors soldered within the heater area to measure the average temperature across the heater, which coincides with the temperature at the heat sink's base surface. A free-hanging type thermistor is secured with tape at the top surface. Temperature readings were collected every 5 s.

Experiments were carried out under atmospheric pressure and various levels of vacuum, specifically (a) 103 500 Pa (ATM), (b) 51 325 Pa, (c) 5 Pa, and (d) 0.00025 Pa. The tests were conducted in the laboratories of the University of Technology Sydney, except for (d) 0.00025 Pa. A vacuum chamber with integrated vacuum pump maintained the desired pressure level throughout the tests. The chamber operated at either the its nominal vacuum rating of 5 Pa (−1 bar(g)) or at half of this rating, at 51 325 Pa (−0.5 bar(g)). The target vacuum level was manually controlled by activating the vacuum pump until the required pressure was reached, monitored via visual inspection of a pressure gauge installed on the chamber. The high-grade vacuum tests at 0.00025 Pa were conducted inside the Wombat-XL thermal vacuum chamber (TVAC), located in the National Space Test Facility in Canberra Australia. Infrared thermal imaging was also captured during the high-grade vacuum tests, to visualise the temperature distribution of the experimental hardware, as well as its vicinity. For the atmospheric pressure (a) and low-grade vacuum tests (b)–(c), the ambient temperature was maintained at 23 °C+/−1.5 °C. The high-grade vacuum test (d) was performed under temperatures ranging from −40 °C to −18 °C, as presented in Section 3.

The PCB and micro-controller were powered by a 5 V portable battery during the atmospheric pressure and low-grade vacuum tests. For the high-grade vacuum experiment, a benchtop power supply provided 5 V into the circuit. The heater operates using pulse width modulation (PWM) signals. Experiments were carried out at two power levels: 100% duty cycle and 50% duty cycle. At 100% duty, the heater remains continuously on, whereas at 50% duty cycle, it switches between on and off states for 50% of the pulse period, providing 50% average power output, as indicated in Eq. (1). Heater power P_{heater} was calculated by Eq. (1) based on the voltage (U) across the heater and its resistance(R). The voltage was measured with a multimeter, recording 4.8 V for the atmospheric pressure and low-grade vacuum tests, and 4.2 V for the high-grade vacuum experiments inside the Wombat-XL TVAC chamber. The heater resistance R was recorded at different temperatures to determine its relationship with temperature T [°C], which is outlined in Eq. (2).

$$P_{heater} = (duty\%)\frac{U^2}{R} \tag{1}$$

$$R = 0.0192T + 2.7774 \tag{2}$$

At the start of each experiment, the test rig was at 23 °C for the atmospheric pressure and low-grade vacuum tests at both 100% and 50% duty, yielding initial heater powers of 7.0 W and 3.5 W, respectively, from Eq. (1). For the high-grade vacuum tests, the heat sink and heater initial temperature was 7 °C at 100% duty, resulting in an initial power of 6.3 W. At 50% duty, the initial temperature was around 35 °C, equivalent to 2.6 W initial P_{heater}. These power levels selected represent realistic operating conditions of CubeSat electronics, which often alternate between high-power active mode such as payload operation and data transmission, and low-power standby mode [25–27].

It was observed during the experiments through thermal imaging that part of P_{heater} escapes through the mounting assembly and, therefore, the actual power input at the base of the heat sink is in fact lower than P_{heater}. The power generated by the heater P_{heater} is partly stored and dissipated by the heat sink ($P_{heatsink}$), and partly lost through the mounting assembly, P_{loss}, as expressed in Eq. (3). $P_{heatsink}$ was calculated for each case according to Eqs. (4), (5), (6), (7), where

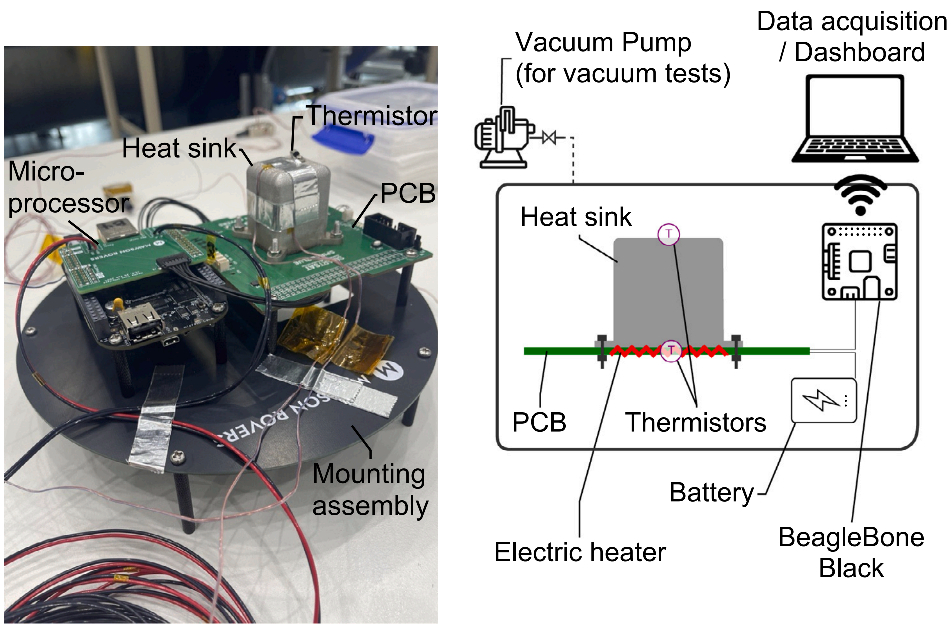

(a) (b)

Fig. 2. (a) Experimental setup picture and (b) corresponding diagram.

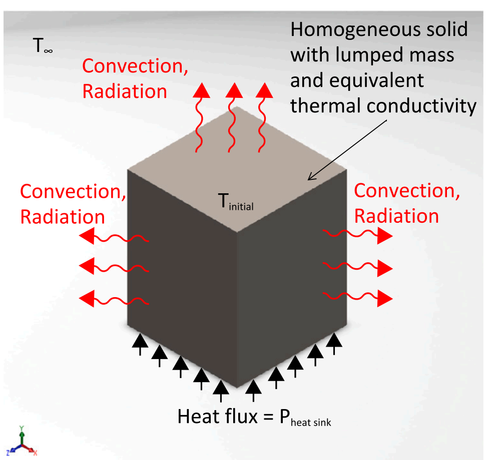

Fig. 3. Initial and boundary conditions.
Source: Adapted from [17].

$\Delta\dot{E}_{heatsink,stored}$ represents the variation in thermal energy stored in the heat sink over a period of time t, and $q_{heatsink,conv}$ and $q_{heatsink,rad}$ correspond to the power dissipated from the external surfaces of the heat sink to the ambient via convective and radiative heat transfer, respectively. A similar approach has been employed by [28]. $P_{heatsink}$ was then calculated as a moving average of each time point. The ratio of $P_{heatsink}$ by P_{heater} was then fitted into a linear function of the temperature difference $T_{base}-T_{\infty}$, established through linear regression. $P_{heatsink}/P_{heater}$ was used as a multiplier to P_{heater} in the numerical simulation, as described in Section 2.2, to represent the actual heat flux supplied at base of the heat sink more accurately.

$$P_{heater} = P_{heatsink} + P_{loss} \tag{3}$$

$$P_{heatsink} = \Delta\dot{E}_{heatsink,stored} + q_{heatsink,conv} + q_{heatsink,rad} \tag{4}$$

$$\Delta\dot{E}_{heatsink,stored} = \frac{mC_p(T_{avg} - T\infty)}{t} \tag{5}$$

Table 1
Uncertainty analysis results.

Quantity	Instrument	Uncertainty (%)	Uncertainty (σ)
Voltage	Multimeter	±1.5%	±0.07 V
Resistance	Multimeter	±0.5%	±0.02 Ω
Temperature	Thermistor	±1.0%	±0.25–1 °C
Power	Dependent variable	± 2.9%	± 0.21 W

$$q_{heatsink,conv} = hA(T_{avg,t_{i+1}} - T_{avg,t_i}) \tag{6}$$

$$q_{heatsink,rad} = \epsilon\sigma A(T_{avg}^4 - T_{\infty}^4) \tag{7}$$

where T_{avg} is the average temperature of the heat sink, simplified as the average between T_{base} and T_{top}, and A is the external surface area of the heat sink. A thermal emissivity ϵ of 0.5 was assigned to the heat sink walls, adapted from [29], considering the high surface roughness resulting from the laser powder bed fusion manufacturing process.

2.1.1. Uncertainty analysis

Table 1 presents the measurement uncertanties for the quantities used in this study. Power uncertainty (Eq. (8)) was derived from the independent quantities voltage and resistance, based on the worst-case scenario, specifically highest voltage of 4.8 V and lowest resistance of 3.2 Ω at 23 °C:

$$\delta_P = \sqrt{\left(\frac{\partial P}{\partial U}\cdot\sigma_U\right)^2 + \left(\frac{\partial P}{\partial R}\cdot\sigma_R\right)^2} = \sqrt{\left(\frac{2U}{R}\cdot\sigma_U\right)^2 + \left(-\frac{U^2}{R^2}\cdot\sigma_R\right)^2} \tag{8}$$

2.1.2. Test procedure

The heat sink sits on top of the heater and was attached to the PCB with nylon bolts and nuts. A coat of Apiezon H thermal grease was used between the heater and the heat sink to enhance thermal contact between the surfaces, since a proper interface is essential for satisfactory performance of heat sinks [30]. The heater was switched on for 60 min and cooling was recorder for 60 min. The experiments conducted are listed in Table 2.

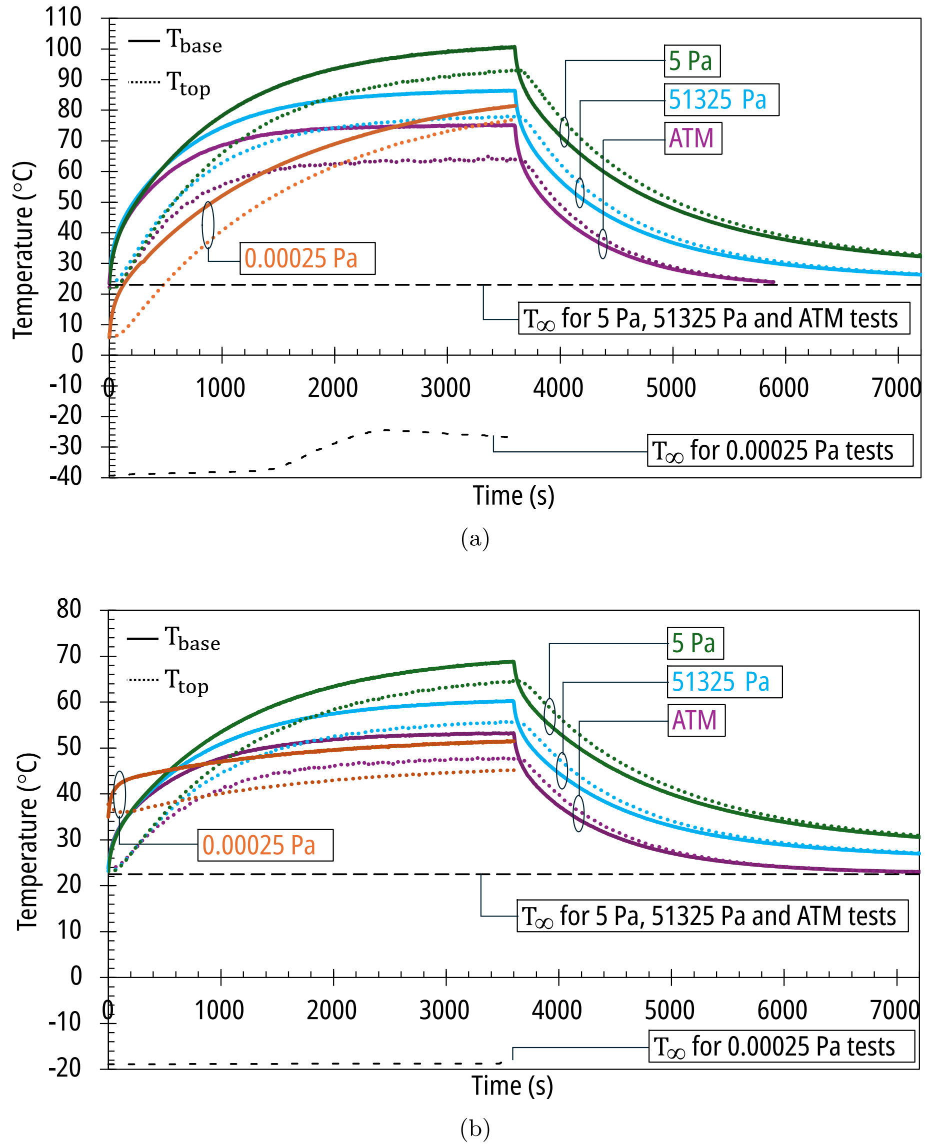

Fig. 4. Experimental results: transient temperatures for heater duties of (a) 100% and (b) 50% at atmospheric pressure (ATM), low-grade vacuum (5 Pa and 51 325 Pa) and high-grade vacuum (0.00025 Pa).

Table 2
Variants of the experiments.

Experiment	Pressure	T_∞	Heater duty
1	Atmospheric pressure (a)	23 °C	100%
2	Atmospheric pressure (a)	23 °C	50%
3	51325 Pa (b)	23 °C	100%
4	51325 Pa (b)	23 °C	50%
5	5 Pa (c)	23 °C	100%
6	5 Pa (c)	23 °C	50%
7	0.00025 Pa (d)	−40 to −20 °C	100%
8	0.00025 Pa (d)	−18 °C	50%

2.2. Reduced-order numerical modelling

Low-complexity numerical modelling was used to forecast the operation of heat sinks across multiple pressures, while requiring relatively low computational efforts. The model, which was verified with this work's experimental results, was based on the assumption of a uniform solid with an equivalent thermal conductivity, k_{eff}. Comparable methodologies have been reported in the literature [17,31–33]. The uniform solid's effective thermal conductivity, k_{eff}, was calculated with a series-parallel method from Eq. (9) [34,35]. The studied heat sink has a ratio between the void volume (V_{void}) and total volume (V_{total}) of 40%, which yields an equivalent thermal conductivity k_{eff} of 9.4 W/mK. This figure was experimentally validated using the approach described in Sueza Raffa, et al. 2024 [17]. A known heat flux was applied into the heat sink with insulated walls and the temperature gradient across its height was measured under steady-state conditions. The effective thermal conductivity was determined through Fourier's law for 1D conduction. While finned structures may exhibit anisotropic thermal behaviour, this study adopts a simplified representation of the heat sink as a homogeneous isotropic solid. This assumption was made to enable the development of a reduced-order model that prioritises computational efficiency without significantly compromising predictive accuracy. Similar simplifications have been used in the literature for space thermal management applications [31,32]. The experimental validation confirms that this approach yields reliable results for the purposes of this study.

$$k_{eff} = \frac{k_{metal} V_{metal} + k_{air} V_{void}}{V_{total}} \tag{9}$$

Numerical simulations. Finite element method calculations were performed with ANSYS Fluent 2021. A custom material with the effective

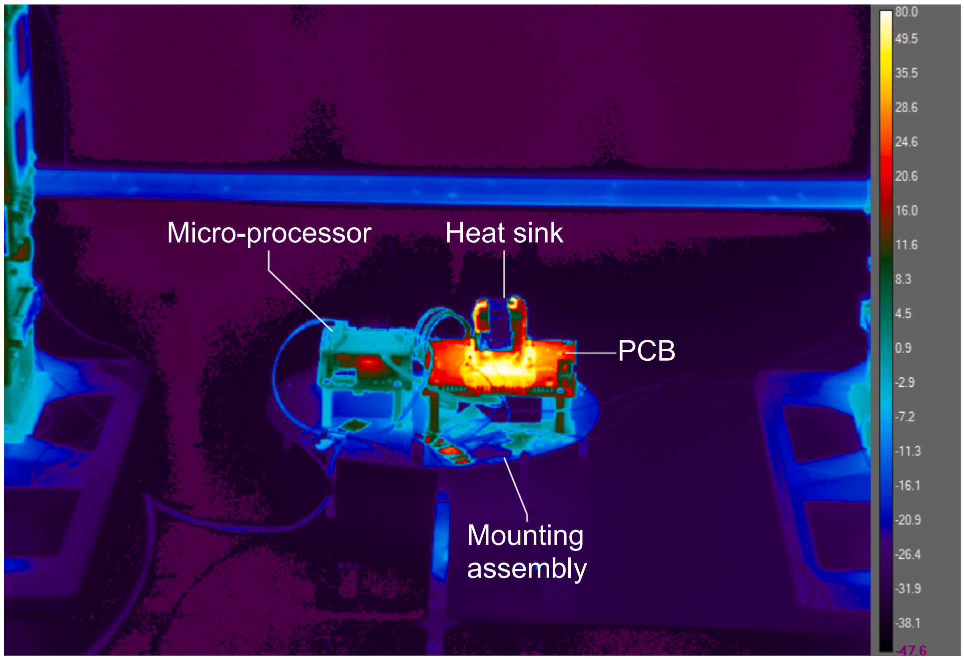

Fig. 5. Thermal image of experimental setup under high-grade vacuum, 100% heater duty, approximately 1500 s.

Table 3
Material properties [36].

Material	Density (kg/m^3)	Specific heat capacity C_p (J/kg K)	Thermal conductivity (W/mK)
SS316L	8000	500	16.3
Effective composite (custom)	4528	500	9.4

thermal conductivity determined from Eq. (9) was created in ANSYS for the effective composite. The density of the homogeneous solid was obtained from the ratio of the mass of the heat sink by its total external volume. The specific heat capacity of stainless steel shown in Table 3 was used.

In the simulations at atmospheric pressure (a) and low-grade vacuum (b)–(c), both convection and radiation dissipation were considered at the heat sink surface. The low-grade vacuum simulations were assigned low-magnitude convection heat transfer coefficients to the boundary condition in the walls to account for the reduced pressure within the vacuum chamber. In the high-grade vacuum simulation (d), only radiation dissipation was considered in the walls. The reduced-order simulations focused on the heat transfer across the solid homogeneous body. For this reason, the flow equation was turned off, with only the Energy equation left for solving. The governing equations are described below:

Transient heat conduction inside solid body:

$$\rho_{eff} C_p \frac{\partial T}{\partial t} = k_{eff} \left(\frac{\partial^2 T}{\partial x^2} + \frac{\partial^2 T}{\partial y^2} + \frac{\partial^2 T}{\partial z^2} \right) \tag{10}$$

Boundary condition at the heat sink surface - Convection:

$$-k_{eff} \frac{\partial T}{\partial n} = hA(T_{\text{heat sink}} - T_\infty) \tag{11}$$

Boundary condition at the heat sink surface - Radiation:

$$-k_{eff} \frac{\partial T}{\partial n} = \epsilon\sigma A \left(T^4_{\text{heat sink}} - T^4_\infty \right) \tag{12}$$

The terms ρ_{eff}, C_p and k_{eff} denote the density, specific heat capacity, and the thermal conductivity of the homogeneous solid created.

The initial and boundary conditions below are shown in Fig. 3:

1. Initial temperature of solid: 23 °C for atmospheric and low-grade vacuum tests; 7 °C for high-grade vacuum simulation at 100% duty; and 33 °C for high grade vacuum simulation at 50% duty.
2. Ambient temperature: 23 °C for atmospheric and low-grade vacuum tests; tabular −40 to −20 °C for high grade vacuum simulations, as plotted in Section 3.
3. Uniform heat flux applied to the base surface of the heat sink as per the heat flux correlation with temperature, as demonstrated in Section 3.3.
4. Walls and top surface heat transfer: via natural convection and radiation for atmospheric pressure and low-grade vacuum simulations, with adjusted convection heat transfer coefficients for the lower pressures; via radiation only for the high-grade vacuum simulations.

The validation of the numerical simulations is detailed in Section 3.3.

3. Results and discussion

The performances of the heat sink across various pressure conditions is analysed using transient thermal response measured at the base and top surfaces of the heat sink, T_{base} and T_{top}. T_{base} coincides with the temperature of the heat-generating electronics, and T_{top} provides insight on the heat rejected to the surroundings and, therefore, is also plotted.

3.1. Experimental work

The experimental results for the transient temperatures T_{base} and T_{top} reveal a significant difference in behaviour based on the pressure condition. The trend is consistent for both 100% and 50% heater duty, as illustrated in Fig. 4, where the higher the operating pressure, the lower the temperatures. However, the trend shifts for the experiments performed under high-grade vacuum in the Wombat-XL TVAC (case (d)), which exhibited a distinct temperature profile due to significantly lower ambient temperatures, as well as reduced heater voltage and power, compared to the tests under atmospheric pressure (a) and low-grade vacuum (b)–(c). The cooling history was not recorded for the

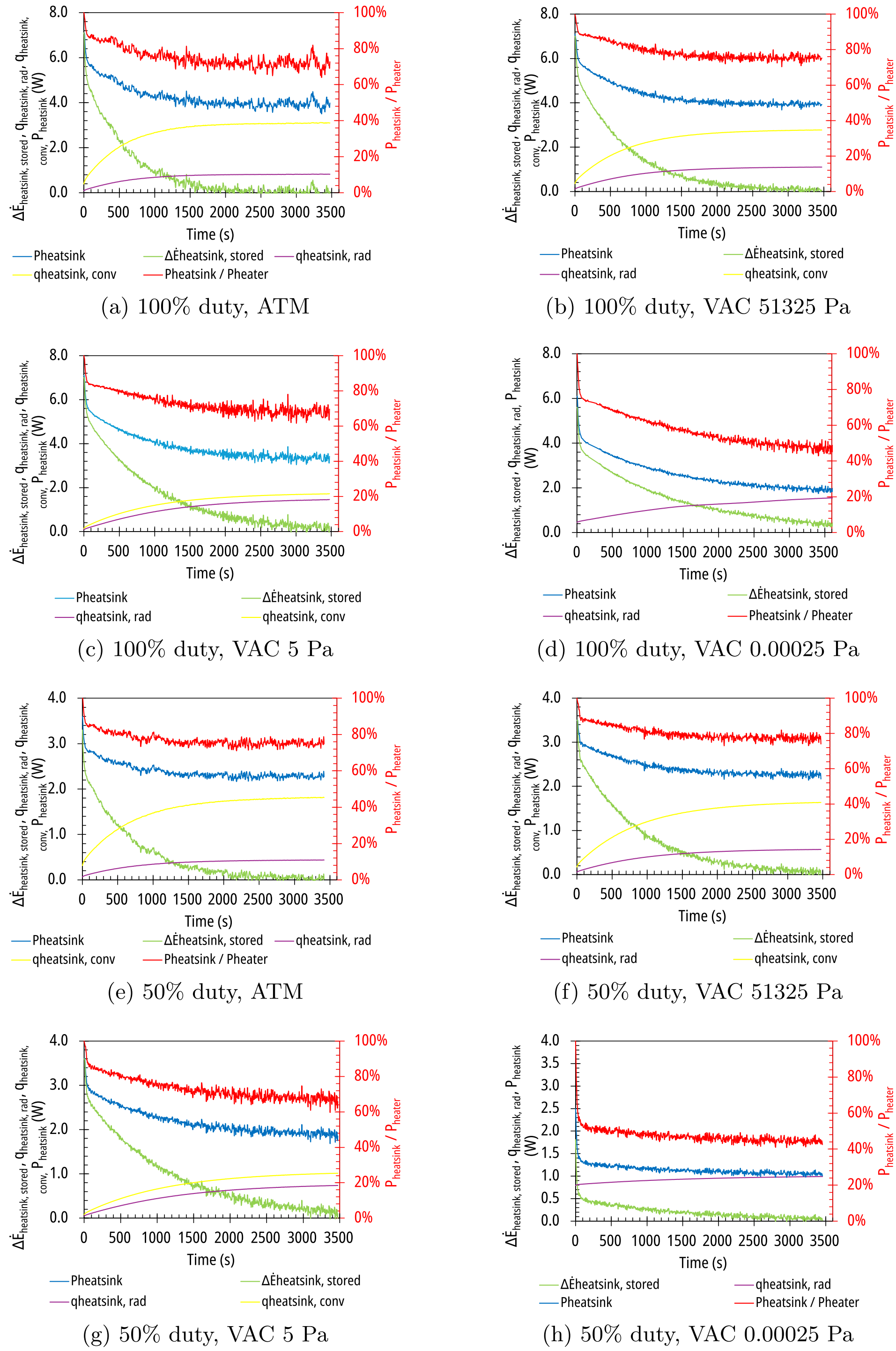

Fig. 6. Calculated $P_{heatsink}$, $P_{heatsink}/P_{heater}$, $\Delta\dot{E}_{heatsink,stored}$, $q_{heatsink,rad}$, and $q_{heatsink,conv}$ for each experiment.

high-grade vacuum (d). To compare across the experimental results from different sites, a finite element analysis (FEA) under high-grade vacuum was performed in Section 3.3 for an ambient temperature of 23 °C, with a heater voltage of 5 V, and including the cooling process. The thermal image captured during the high-grade vacuum test (d) at approximately 1500 s for 100% heater duty, reveals notable thermal losses through the mounting assembly (Fig. 5). At that instant, while the base surface was at approximately 60 °C, the PCB edges, PCB standoffs, and mounting plate were at approximately 25 °C, 15 °C, and −15 °C, respectively. Given the significance of the heat losses through the mounting assembly (P_{loss}), it is essential to determine the useful portion of the heater power, or the actual power transferred to the heat sink ($P_{heatsink}$), for the simulation analysis. The determination of $P_{heatsink}$ is detailed in Section 3.2 to enable capturing these losses.

3.2. Quantification of heat losses through the assembly mount and determination of the actual heat flux into the heat sink

As described in Section 3.1, the actual heat flux applied into the heat sink, $P_{heatsink}$, is the sum of the increment of thermal energy stored in the heat sink, $\Delta\dot{E}_{heatsink}$, and the convective and radiative heat rejected by the heat sink surfaces, $q_{heatsink,conv}$ and $q_{heatsink,rad}$. These parameters

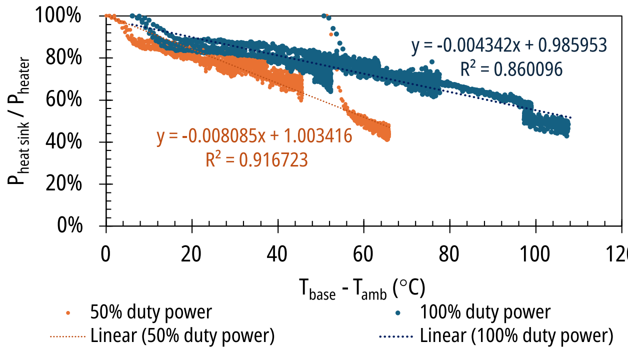

Fig. 7. Calculated $P_{heatsink}/P_{heater}$ from the experimental tests.

were calculated through Eqs. (5), (6), (7) at each time point as a moving average, and are displayed in Fig. 6 for all operating pressures and power settings.

Using the heater power P_{heater} determined through Eq. (1), the ratio $P_{heatsink}/P_{heater}$ was calculated for each time step. This ratio represents the fraction of the total heater power that is effectively applied at the base of the heat sink, excluding any power dissipated through the assembly mount. Fig. 6 shows that the ratio is close to 100% at the beginning and decreases over time, suggesting an increasing power loss though the mounting assembly as the heating duration progresses. The rationale is that, as the heating advances and the heater temperature increases, the temperature difference relative to the ambient, $T_{base} - T_\infty$, grows, leading to greater heat loss through the mounting assembly. The ratio $P_{heatsink}/P_{heater}$, was then plotted against $T_{base} - T_\infty$, revealing a near-linear relation for each power level, as shown in Fig. 7. The alignment of the power losses along the same linear trend across all pressure conditions possibly indicates that heat losses through the assembly mount occur primarily via conduction through the standoffs and supports. A linear expression for $P_{heatsink}/P_{heater}$ was derived using linear regression for each power level. For the numerical simulations, the heat flux applied onto the base of the heat sink, $P_{heatsink}$, was inputted as the expression given by the product between the linear expression for $P_{heatsink}/P_{heater}$ (Fig. 7) and the expression for P_{heater} (Eq. (1)).

Fig. 6 also provides graphical visualisation of the significance of convection and radiation heat dissipation for each pressure level. Interestingly, for 5 Pa (c), which is the nominal vacuum rating of the vacuum pump used, convection and radiation have a similar impact in the heat dissipation to the ambient, suggesting that a small convection heat transfer coefficient shall be considered for simulations under such level of vacuum. The incremental thermal energy stored in the heat sink, $\Delta\dot{E}_{heatsink}$, is also analysed. For both heater duty cycles, the higher the operating pressure, the faster $\Delta\dot{E}_{heatsink}$ approaches zero. Negligible values of $\Delta\dot{E}_{heatsink}$ indicate a steady-state condition, when the rate of heat entering system matches the rate at which it exits it, resulting in stabilisation of temperatures, as observed in Fig. 4.

3.3. Reduced order numerical simulation - Validation

Strong correlation was found between the reduced-order numerical model and the experimental data for all pressure conditions and heater duties, as observed in Fig. 8. The maximum difference between the experimental and numerical base temperatures was 3.2 °C, observed at around 240 s for the high-grade vacuum test at 100% duty power. For the 50% duty tests, the maximum difference was 1.5 °C, also around 240 s for high-grade vacuum. This demonstrates this simplified model, which requires low computational effort, is an effective tool for estimating the transient temperatures of heat sinks with specified porosity across various pressure levels.

3.4. Comparison of the heat sink performance under multiple pressure conditions at the same ambient temperature

As pointed out in Section 3.1, the high-grade vacuum tests were performed for different ambient and initial temperatures, and with a different heater voltages in relation to the atmospheric and low-grade vacuum tests. Hence, for a consistent comparison, in which the ambient and initial temperatures, and the heater voltage coincide across all pressure levels, a simulation was performed for high-grade vacuum to mimic the experimental setup of the low grade vacuum tests. This simulation used ambient and initial temperatures of 23 °C, and a heater voltage of 4.8 V. The results of these simulations are juxtaposed with the experiments for atmospheric pressure and low-grade vacuum, as shown in Fig. 9.

At the beginning of heating, the base temperatures increased nearly at the same rate for all operating pressures up to approximately 52 °C (around 300 s) for 100% duty power, and up to around 38 °C for 50% duty power. During this period, the heat sink likely absorbed the majority of the thermal energy without sufficient dissipation, as most of the heat transfers from the base via conduction, given the relatively high thermal conductivity of the metallic heat sink. In addition, the temperature difference between the heat sink surfaces and the ambient was relatively minor, leading to minimal heat dissipation to the surroundings. Beyond this point, the temperature profiles diverge according to the amount of heat dissipation driven by each pressure level.

A clear distinction across pressure conditions is observed. For both power levels, the tests conducted under atmospheric pressure yielded the lowest base and top temperatures throughout both the heating and cooling processes, primarily due to effective convective heat transfer. Conversely, higher temperatures were observed for lower operating pressures with a monotonically increasing inverse relation between the temperature and pressure, demonstrating the impact of decreased convection. The maximum electronics temperature achieved at atmospheric pressure was 75.1 °C at 100% duty, and 53.2 °C at 50% duty power. Under low-grade vacuum pressures, heat dissipation is proportionally reduced, leading to higher peak temperatures. For the 51 325 Pa tests (−0.5 bar(g)), the electronics reached a maximum of 86.5 °C at 100% duty power, and 60.2 °C at 50% duty. This represents an increase of around 15% at both 100% and 50% duties, relative to atmospheric pressure. For the 5 Pa tests (−1 bar(g)), the maximum temperatures were 100.7 °C at 100%, and 68.8 °C at 50% duty. The jump in relation to atmospheric pressure was in the vicinity of 30%.

Interestingly, the 51 325 Pa cases (−0.5 bar(g)) exhibited base temperatures almost equidistant between the atmospheric pressure (0 bar(g)) and 5 Pa (−1 bar(g)) curves throughout the duration of heating and cooling. This indicates that the convection heat transfer coefficient is directly proportional to the pressure level. The convection heat transfer coefficients utilised in the simulations performed in Section 3.3 to validate the proposed model were indeed proportional to the operating pressure. The adopted values were 15 W/m^2 K, 10 W/m^2 K, and 5 W/m^2 K for atmospheric pressure, −0.5 bar(g) and −1 bar(g), respectively, confirming this direct relation between convection heat dissipation and ambient pressure.

The high-grade vacuum (0.00025 Pa) more accurately simulates actual orbital pressure conditions. Under this operating pressure, the base temperatures peaked at 125 °C at 100% duty, and 83.5 °C at 50% duty. These temperatures were up to 66% higher than those observed at atmospheric pressure. More elevated temperatures for lower pressures are explained by the diminished convective heat transfer, driven by the lower density of air particles, which reduces the buoyancy effect, promoting less efficient heat dissipation. Ultimately, convection heat dissipation becomes negligible under high-pressure vacuum conditions, explaining the more elevated temperatures observed under this pressure level.

The temperatures recorded at the top surface provide insights on its efficiency under varying operating pressures. For both power levels, it

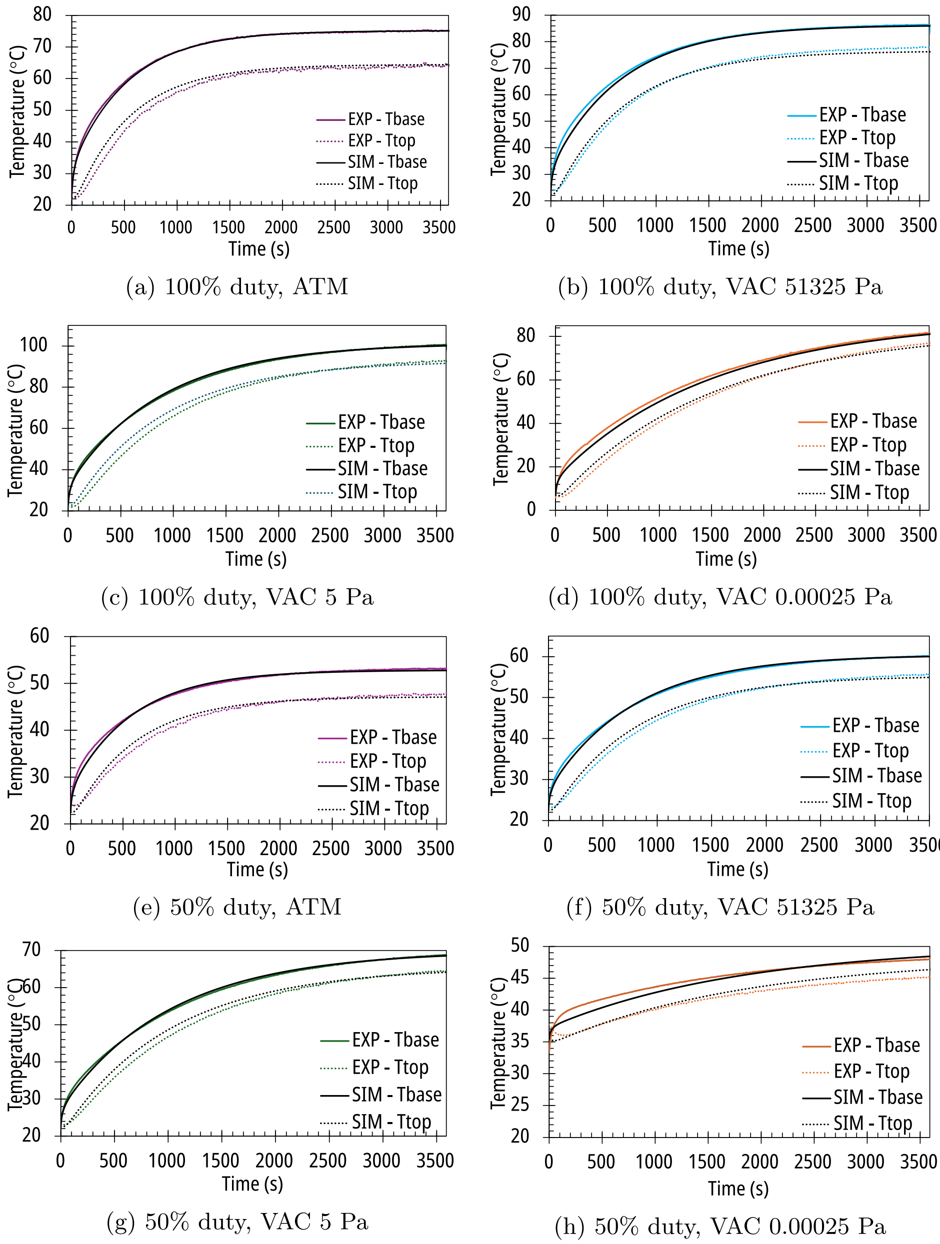

Fig. 8. Validation of the reduced-order numerical model.

was noted that the temperature difference between the base and top surfaces during heating is greater at lower operating pressures. This is consistent with the increased heat dissipation at conditions closer to atmospheric pressure levels.

These results highlight the significant role that ambient pressure plays in the thermal performance of heat sinks, especially in environments with limited or absent convective cooling. Future investigations should prioritise the development of thermal management solutions tailored to address these pressure-dependent behaviours, enhancing the reliability and effectiveness of heat sinks for space applications.

4. Conclusion

This work demonstrates the significant influence of ambient pressure on the thermal performance of stainless steel heat sinks, with electronics temperatures increasing as pressure decreases. Low-grade vacuum conditions (51 325 Pa and 5 Pa) sustain temperatures approximately 15 to 30% higher than at atmospheric pressure. For high-grade vacuum (0.00025 Pa), the increase in temperature was close to 70% compared to atmospheric pressure. The relationship between pressure and convective heat transfer was evident, with the convection heat transfer coefficient being directly proportional to the pressure level, until convection dissipation is entirely neglected for high-vacuum conditions. It was determined convection in typical off the shelf vacuum systems (5 Pa) still plays a role as significant as radiation and cannot be overlooked. Therefore, to achieve a closer "test like you fly" approach in designing and developing thermal management solutions for satellites, an ability to test under a high-grade thermal vacuum chamber like the Wombat-XL is crucial.

The reduced-order numerical model proved to be an effective tool for predicting transient heat sink behaviour across different pressure environments. A strong correlation between the experimental and simulation results validates the model's capability to reproduce the thermal behaviour of stainless steel heat sinks under varying conditions of ambient temperature and pressure. This model can be extended to predict the thermal performance of similar metallic heat sink designs in orbit. It

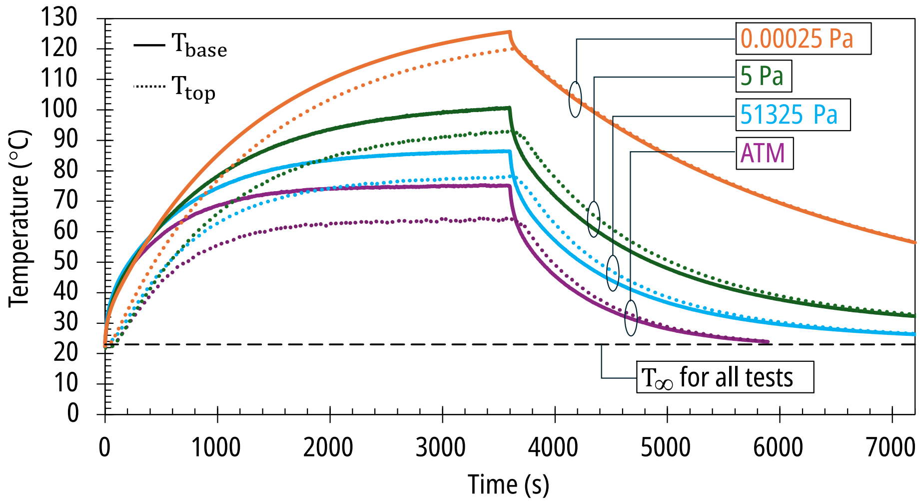

(a) 100% duty

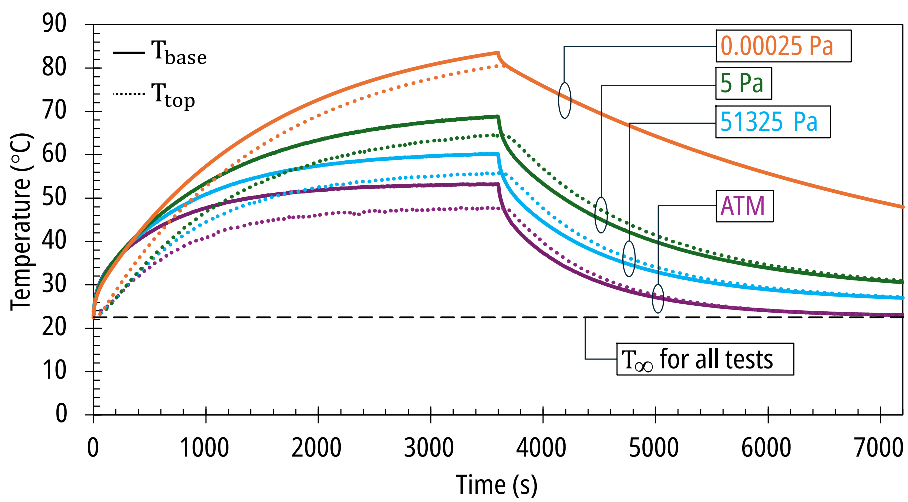

(b) 50% duty

Fig. 9. Transient temperature for heater duties of (a) 100% and (b) 50% - All cases at the same ambient and initial temperature and heater voltage. Note: The results shown for atmospheric pressure (ATM) and low-grade vacuum (5 Pa and 51 325 Pa) were obtained experimentally, and the high-grade vacuum (0.00025 Pa) curves result from the numerical simulations at 23 °C ambient and initial temperature and 4.8 V across the heater to ensure comparability with the atmospheric and low-grade vacuum experimental results for these same conditions.

can also be adapted to other thermal management systems applications, such as microprocessors and satellite electronics, providing a valuable tool for space systems design and optimisation.

The findings of this work emphasise the need for thermal management strategies for space applications where convective cooling is absent, given that the operation of passive thermal management modules in vacuum conditions is not significantly detailed in the literature. The findings also indicate that heat sinks designed for terrestrial use may underperform in space unless optimised for vacuum conditions. Effective thermal management in such environments requires heat sink designs that promote efficient conduction and radiation. Key design considerations include increasing the radiative surface area, optimising fin geometry to maximise view factors, applying high-emissivity coatings, and integrating phase change materials (PCMs) to buffer peak thermal loads. Material selection should also be selected to balance the required thermal conductivity and mass constraints. These adaptations are essential to ensure thermal reliability of satellite avionics and payloads in the space environment. Future research should explore innovative solutions such as phase change materials with tailored heat sink geometries, and explore alternative materials with different thermal conductivities to enhance performance. Additionally, more extensive testing across a broader range of pressure conditions to establish a general correlation between ambient pressure and convection heat transfer coefficient would further support the design of thermal systems.

CRediT authorship contribution statement

Laryssa Sueza Raffa: Writing – original draft, Validation, Project administration, Methodology, Investigation, Formal analysis, Data curation, Conceptualization. **Matt Ryall:** Software, Resources. **Iver Cairns:** Writing – review & editing, Resources. **Nick S. Bennett:** Writing – review & editing, Supervision. **Lee Clemon:** Writing – review & editing, Supervision.

Declaration of competing interest

The authors declare the following financial interests/personal relationships which may be considered as potential competing

interests: Laryssa Sueza Raffa reports financial support was provided by Australian Government Research Training Program. Nick Bennett reports financial support was provided by SmartSat Cooperative Research Centre. Laryssa Sueza Raffa reports financial support was provided by University of Technology Sydney. Laryssa Sueza Raffa reports financial support was provided by Australian Research Council Training Centre for CubeSats, UAVs, and Their Applications. Laryssa Sueza Raffa reports financial support was provided by Waratah Seed Project, partially funded by Investment NSW. If there are other authors, they declare that they have no known competing financial interests or personal relationships that could have appeared to influence the work reported in this paper.

Acknowledgements

This research was funded by the University of Technology Sydney, the SmartSat Cooperative Research Centre, the Australian Research Council Training Centre for CubeSats, UAVs, and Their Applications (CUAVA) via grant IC170100023, the Waratah Seed project - partially funded by Investment NSW -, and the Australian Government Research Training Program. The authors extend their gratitude to the National Space Test Facility at The Australian National University (ANU) for facilitating the thermal performance tests conducted in the Wombat-XL thermal vacuum chamber, with special thanks to Dr Eduardo Trifoni. Last but not least, they sincerely appreciate Dr Xueliang Bai and Mr Patrick Oppel from CUAVA for their valuable assistance during these experiments.

Data availability

Data will be made available on request.

References

[1] S. Selvadurai, A. Chandran, D. Valentini, B. Lamprecht, Passive thermal control design methods, analysis, comparison, and evaluation for micro and nanosatellites carrying infrared imager, Appl. Sci. 12 (6) (2022) 2858, http://dx.doi.org/10.3390/app12062858, URL https://www.mdpi.com/2076-3417/12/6/2858.

[2] Y.A. Çengel, Heat and mass transfer: A practical approach, in: McGraw-Hill Series in Mechanical Engineering, third ed., McGraw-Hill, Boston, 2007.

[3] Z. Wan, G. Guo, K. Su, Z. Tu, W. Liu, Experimental analysis of flow and heat transfer in a miniature porous heat sink for high heat flux application, Int. J. Heat Mass Transfer 55 (15–16) (2012) 4437–4441, http://dx.doi.org/10.1016/j.ijheatmasstransfer.2012.04.013, URL https://linkinghub.elsevier.com/retrieve/pii/S0017931012002566.

[4] K.K. Baraya, Thermal management challenges in small satellites, in: V.K. Singh, G. Choubey, S. Suresh (Eds.), Advances in Thermal Sciences, in: Lecture Notes in Mechanical Engineering, Springer Nature Singapore, Singapore, 2023, pp. 217–229, http://dx.doi.org/10.1007/978-981-19-6470-1_18, URL https://link.springer.com/10.1007/978-981-19-6470-1_18.

[5] S.A. Jacklin, Small-satellite mission failure rates, 2019.

[6] H.-S. Seo, J. Rhee, E.-S. Han, I.-S. Kim, Thermal failure of the LM117 regulator under harsh space thermal environments, Aerosp. Sci. Technol. 27 (1) (2013) 49–56, http://dx.doi.org/10.1016/j.ast.2012.06.006, URL https://linkinghub.elsevier.com/retrieve/pii/S1270963812001046.

[7] X. Wang, W. Deng, X. Tang, H. He, Experiment and simulation study on the specification parameters of finned heat sink for thermoelectric system in consideration of radiation among fins, Int. J. Therm. Sci. 185 (2023) 108097, http://dx.doi.org/10.1016/j.ijthermalsci.2022.108097, URL https://linkinghub.elsevier.com/retrieve/pii/S1290072922006251.

[8] I. El Ghandouri, A. El Maakoul, S. Saadeddine, M. Meziane, I. Dhriss, Comparison of thermal performance of plate and corrugated fin heatsinks with a modified base under free convection, Mater. Today: Proc. 66 (2022) 100–108, http://dx.doi.org/10.1016/j.matpr.2022.03.676, URL https://linkinghub.elsevier.com/retrieve/pii/S2214785322020557.

[9] M.A. Rahman, S.M.M. Hasnain, P. Paramasivam, A.G. Ayanie, Advancing thermal management in electronics: A review of innovative heat sink designs and optimization techniques, RSC Adv. 14 (43) (2024) 31291–31319, http://dx.doi.org/10.1039/D4RA05845C, URL https://xlink.rsc.org/?DOI=D4RA05845C.

[10] V. Nair, A. Baby, A. M.B., I. S., M. Murali, M.B. Nair, A comprehensive review of air-cooled heat sinks for thermal management of electronic devices, Int. Commun. Heat Mass Transfer 159 (2024) 108055, http://dx.doi.org/10.1016/j.icheatmasstransfer.2024.108055, URL https://linkinghub.elsevier.com/retrieve/pii/S0735193324008170.

[11] C.-H. Huang, W.-Y. Chen, A natural convection horizontal straight-fin heat sink design problem to enhance heat dissipation performance, Int. J. Therm. Sci. 176 (2022) 107540, http://dx.doi.org/10.1016/j.ijthermalsci.2022.107540, URL https://linkinghub.elsevier.com/retrieve/pii/S1290072922000795.

[12] Y.K. Khor, Y.M. Hung, B.K. Lim, On the role of radiation view factor in thermal performance of straight-fin heat sinks, Int. Commun. Heat Mass Transfer 37 (8) (2010) 1087–1095, http://dx.doi.org/10.1016/j.icheatmasstransfer.2010.06.012, URL https://linkinghub.elsevier.com/retrieve/pii/S0735193310001351.

[13] R. Adhikari, D. Wood, M. Pahlevani, Optimizing rectangular fins for natural convection cooling using CFD, Therm. Sci. Eng. Prog. 17 (2020) 100484, http://dx.doi.org/10.1016/j.tsep.2020.100484, URL https://linkinghub.elsevier.com/retrieve/pii/S2451904920300068.

[14] S.-H. Yu, D. Jang, K.-S. Lee, Effect of radiation in a radial heat sink under natural convection, Int. J. Heat Mass Transfer 55 (1–3) (2012) 505–509, http://dx.doi.org/10.1016/j.ijheatmasstransfer.2011.09.026, URL https://linkinghub.elsevier.com/retrieve/pii/S0017931011005230.

[15] W.-X. Chu, Y.-C. Lin, C.-Y. Chen, C.-C. Wang, Experimental and numerical study on the performance of passive heat sink having alternating layout, Int. J. Heat Mass Transfer 135 (2019) 822–836, http://dx.doi.org/10.1016/j.ijheatmasstransfer.2019.02.034, URL https://linkinghub.elsevier.com/retrieve/pii/S0017931018357090.

[16] R.E. Seidel, J. Rhee, Parametric study of heat sink performance at high altitudes with air impingement cooling, in: Electronic and Photonic Packaging, Electrical Systems Design and Photonics, and Nanotechnology, ASMEDC, Chicago, Illinois, USA, 2006, pp. 401–407, http://dx.doi.org/10.1115/IMECE2006-15522, URL https://asmedigitalcollection.asme.org/IMECE/proceedings/IMECE2006/47691/401/321126.

[17] L.S. Raffa, N.S. Bennett, M. Ryall, L.M. Clemon, Experimental investigation of the performance of a phase change material thermal management module under vacuum and atmospheric pressure conditions, Int. J. Heat Mass Transfer (2024) http://dx.doi.org/10.2139/ssrn.4932140, URL https://www.ssrn.com/abstract=4932140.

[18] W. Palm, C. Stone, Test like you fly-implications for R&D systems, in: AIAA 2009-1750, American Institute of Aeronautics and Astronautics, Albuquerque, New Mexico, 2009, pp. 1–7, http://dx.doi.org/10.2514/6.2009-1750.

[19] Q. Wang, Q. Gu, S. Yan, G. Wang, B. Yuan, H. Li, Radiation cooling for heat sinks with high emissivity lanthanum aluminate ceramic coating, Ceram. Int. 49 (20) (2023) 32470–32477, http://dx.doi.org/10.1016/j.ceramint.2023.07.209, URL https://linkinghub.elsevier.com/retrieve/pii/S0272884223021491.

[20] H. Zu, W. Dai, Y. Li, K. Li, J. Li, Analysis of enhanced heat transfer on a passive heat sink with high-emissivity coating, Int. J. Therm. Sci. 166 (2021) 106971, http://dx.doi.org/10.1016/j.ijthermalsci.2021.106971, URL https://linkinghub.elsevier.com/retrieve/pii/S129007292100137X.

[21] D. Jafari, W.W. Wits, The utilization of selective laser melting technology on heat transfer devices for thermal energy conversion applications: A review, Renew. Sustain. Energy Rev. 91 (2018) 420–442, http://dx.doi.org/10.1016/j.rser.2018.03.109, URL https://linkinghub.elsevier.com/retrieve/pii/S1364032118302004.

[22] G. Miranda, S. Faria, F. Bartolomeu, E. Pinto, S. Madeira, A. Mateus, P. Carreira, N. Alves, F. Silva, O. Carvalho, Predictive models for physical and mechanical properties of 316L stainless steel produced by selective laser melting, Mater. Sci. Eng.: A 657 (2016) 43–56, http://dx.doi.org/10.1016/j.msea.2016.01.028, URL https://linkinghub.elsevier.com/retrieve/pii/S0921509316300272.

[23] A.N. Pilagatti, G. Piscopo, E. Atzeni, L. Iuliano, A. Salmi, Design of additive manufactured passive heat sinks for electronics, J. Manuf. Process. 64 (2021) 878–888, http://dx.doi.org/10.1016/j.jmapro.2021.01.035, URL https://linkinghub.elsevier.com/retrieve/pii/S1526612521000542.

[24] M. Arqam, L.S. Raffa, S. Spisiak, L. Clemon, Z. Luo, M. Ryall, M.S. Islam, N.S. Bennett, Computational and experimental analysis of a novel triply periodic minimal surface heat sink with phase change material, J. Energy Storage 117 (2025) 116121, http://dx.doi.org/10.1016/j.est.2025.116121, URL https://linkinghub.elsevier.com/retrieve/pii/S2352152X25008345.

[25] D. Gilmore, Spacecraft Thermal Control Handbook, Volume I: Fundamental Technologies, American Institute of Aeronautics and Astronautics, Inc., Washington, DC, 2002, http://dx.doi.org/10.2514/4.989117, URL https://arc.aiaa.org/doi/book/10.2514/4.989117.

[26] S.-J. Kang, H.-U. Oh, On-orbit thermal design and validation of 1 U standardized CubeSat of STEP cube lab, Int. J. Aerosp. Eng. 2016 (2016) 1–17, http://dx.doi.org/10.1155/2016/4213189, URL http://www.hindawi.com/journals/ijae/2016/4213189/.

[27] S. Isaacs, D.A. Arias, G. Shoukas, Development of a lightweight and low-cost 3D-printed aluminum and PCM panel for thermal management of CubeSat applications, in: ICES-2017-108, 2017, pp. 1–15.

[28] S. Taylor, N. Boman, J. Chao, L. Wang, Cryothermal vacuum measurement of thermochromic variable-emittance coatings with heating/cooling hysteresis for spacecraft thermal management, Appl. Therm. Eng. 199 (2021)

117561, http://dx.doi.org/10.1016/j.applthermaleng.2021.117561, URL https://linkinghub.elsevier.com/retrieve/pii/S1359431121009911.

[29] G. Mohr, S. Nowakowski, S.J. Altenburg, C. Maierhofer, K. Hilgenberg, Experimental determination of the emissivity of powder layers and bulk material in laser powder bed fusion using infrared thermography and thermocouples, Metals 10 (11) (2020) 1546, http://dx.doi.org/10.3390/met10111546, URL https://www.mdpi.com/2075-4701/10/11/1546.

[30] E. Ajul, S. Chanda, Estimation of thermal contact conductance of spacecraft heat sink bolted joints, Appl. Therm. Eng. 224 (2023) 120078, http://dx.doi.org/10.1016/j.applthermaleng.2023.120078, URL https://linkinghub.elsevier.com/retrieve/pii/S1359431123001072.

[31] K. Swaminathan Gopalan, V. Eswaran, Numerical investigation of thermal performance of PCM based heat sink using structured porous media as thermal conductivity enhancers, Int. J. Therm. Sci. 104 (2016) 266–280, http://dx.doi.org/10.1016/j.ijthermalsci.2016.01.008, URL https://linkinghub.elsevier.com/retrieve/pii/S1290072916000168.

[32] Y. Guo, H. Yang, G. Lin, H. Jin, X. Shen, J. He, J. Miao, Thermal performance of a 3D printed lattice-structure heat sink packaging phase change material, Chin. J. Aeronaut. 34 (5) (2021) 373–385, http://dx.doi.org/10.1016/j.cja.2020.07.033, URL https://linkinghub.elsevier.com/retrieve/pii/S1000936120303551.

[33] S. Du, D. Li, M.-J. Li, Y.-L. He, Numerical study on the effective thermal conductivity and thermal tortuosity of porous media with different morphologies, Sci. China Technol. Sci. 67 (6) (2024) 1685–1694, http://dx.doi.org/10.1007/s11431-023-2481-4, URL https://link.springer.com/10.1007/s11431-023-2481-4.

[34] D.S. Smith, A. Alzina, J. Bourret, B.t. Nait-Ali, F. Pennec, N. Tessier-Doyen, K. Otsu, H. Matsubara, P. Elser, U.T. Gonzenbach, Thermal conductivity of porous materials, J. Mater. Res. 28 (17) (2013) 2260–2272, http://dx.doi.org/10.1557/jmr.2013.179, URL http://link.springer.com/10.1557/jmr.2013.179.

[35] I. Garmendia, H. Vallejo, M. Seco, E. Anglada, Design and fabrication of a phase change material heat storage device for the thermal control of electronics components of space applications, Aerospace 9 (3) (2022) 126, http://dx.doi.org/10.3390/aerospace9030126, URL https://www.mdpi.com/2226-4310/9/3/126.

[36] M. Arqam, L.S. Raffa, L. Clemon, M.S. Islam, M. Ryall, N.S. Bennett, Numerical and experimental investigation of a phase change material radial fin heat sink for electronics cooling, J. Energy Storage 98 (2024) 113113, http://dx.doi.org/10.1016/j.est.2024.113113, URL https://linkinghub.elsevier.com/retrieve/pii/S2352152X24026999.